1   Ice Crystal Concentrations in Wave Clouds: Dependencies on Temperature, D>0.5 µm

2   Aerosol Particle Concentration and Duration of Cloud Processing

3

4   L.Peng, J.R. Snider and Z. Wang

5

6   Corresponding author: J.R. Snider

7   Department of Atmospheric Sciences

8   University of Wyoming, Laramie, WY

9

10   **Abstract**

11

12   Model equations used to either diagnose or prognose the concentration of

13   heterogeneously nucleated ice crystals depend on combinations of cloud temperature,

14   aerosol properties, and elapsed time of supersaturated-vapor or supercooled-liquid

15   conditions. The validity of these equations is questioned. For example, there is concern

16   that practical limitations on aerosol particle time-of-exposure to supercooled-liquid

17   conditions, within ice nucleus counters, can bias model equations that have been

18   constrained by ice nuclei (IN) measurements. In response to this concern, this work

19   analyzes airborne measurements of crystals made within the downwind glaciated portions

20   of wave clouds. A streamline model is used to connect a measurement of aerosol

21   concentration, made upwind of a cloud, to a downwind ice crystal (IC) concentration.

22   Four parameters were derived for 80 streamlines: (1) minimum cloud temperature along

23   the streamline, (2) aerosol particle concentration (diameter, $D > 0.5$ μm) measured within

24   ascending air, upwind of the cloud, (3) IC concentration measured in descending air

25   downwind, and (4) the duration of water-saturated conditions along the streamline. The

26   latter are between 38 to 507 s and the minimum temperatures are between -34 to -14 ^{o}C.

27   Values of minimum temperature, $D > 0.5$ μm aerosol concentration and IC concentration

28   were fitted using the equation developed for IN by DeMott et al. (2010; D10). Overall,

29   there is reasonable agreement among measured IC concentrations, IN concentrations

30   derived using D10's fit equation, and IC concentrations derived by fitting the wave cloud

31   measurements with the equation developed by D10.

32

1 - Introduction

Ice nucleation is a pivotal process in the evolution of many cloud types [Braham and Squires, 1974; Cantrell and Heymsfield, 2005; DeMott et al., 2010; Murray et al., 2012]. Ice crystals form via different pathways; the two fundamental distinctions are homogeneous and heterogeneous nucleation. Temperatures colder than -35 °C, and the existence of either haze particles or cloud droplets, are necessary conditions for the occurrence of the homogeneous pathway [Heymsfield and Miloshevich, 1993]. Heterogeneous ice nucleation takes place on aerosol particles (ice nuclei, IN) and the known pathways are deposition, condensation freezing, immersion freezing and contact freezing [Vali, 1985; Murray et al., 2012].

Two contrasting approaches are used to translate measurements into equations used to predict IN activation, and thus ice crystal (IC) concentration, in cloud models. The first of these is diagnostic in the sense that IC concentration is formulated solely in terms of thermodynamic and aerosol state properties. The second is state and time dependent. In model intercomparison studies [Eidhammer et al., 2009; Niemand et al., 2012], these two frameworks produce significantly different IC concentrations. There are many reasons for these inconsistencies; fundamentally, they result because the time scale characterizing the development of a subcritical ice embryo into an ice crystal [Bigg, 1953; Vali and Stansbury, 1966], and how properties of an aerosol particle influences embryo development, are inadequately understood [Murray et al., 2012; Vali, 2014]. Another relevant factor, but one which attenuates the framework-to-framework differences [Eidhammer et al., 2009], is that the Bergeron-Findeisen process can act to

55   slow, or even shut down, the freezing nucleation pathways (i.e., condensation, immersion

56   and contact freezing).

57   Our primary focus is the temperature- and aerosol-dependent IN fit equation

58   developed by DeMott et al. (2010; hereafter D10). The D10 equation, hereafter Eqn. 1,

59   was developed with measurements of activated IN concentration derived using the

60   continuous flow diffusion chamber (CFDC; Rogers et al., 2001). The IN measurements

61   were made concurrently with measurements of the concentration of aerosol particles with

62   diameter (D) larger than 0.5 µm ($n_{0.5}$)

63    $$N_{IN}(T, n_{0.5}) = a \cdot (T_O - T)^b \cdot (n_{0.5})^{c \cdot (T_O - T) + d}. \qquad (1)$$

64   Here T is the temperature in the section of the CFDC operated above water saturation,

65   T_O is a reference temperature (273.16 K), and a, b, c and d are the fitted coefficients.

66   We reexamine Eqn. 1 because it was developed with the CFDC operating in a manner

67   which restricted the upper-limit diameter of aerosol particles processed within the CFDC

68   ($D < 1.6$ µm) and which restricted the duration of the particle's exposure to water-

69   saturated conditions ($t < 10$ s). Since both of these restrictions can cause the IN

70   concentration to be underestimated (D10; Wright et al., 2013; DeMott et al., 2014), we

71   use measurements made in and near clouds to evaluate the potential bias.

72   We have three specific objectives. First we use our airborne measurements of IC

73   concentration to derive a temperature-dependent fit of those measurements. We refer to

74   these two properties as N_{IC} and $N_{IC}(T)$, respectively. Specifically, we analyze IC

75   concentrations recorded within the downwind (descending flow) portion of middle-

76   tropospheric wave clouds, where IC concentration is thought to reflect IN activation that

77   occurred upwind, within the colder and liquid-water saturated portion of the cloud.

78 Second, we use our measurements to derive a temperature- and aerosol-dependent fit of

79 N_{IC} based on Eqn. (1). We refer to the latter as $N_{IC}(T, n_{0.5})$. Third, we analyze our

80 measurement of N_{IC} with an estimate of the interval of time an air parcel was exposed

81 to water-saturation within a wave cloud. This is relevant to cloud modeling because many

82 models employ a state- and time-dependent framework to predict IC concentration [e.g.,

83 Hoose et al., 2010].   The IN, aerosol and IC concentrations relevant to our work are

84 summarized in Tab. 1.

85   The foundations of our investigation are the cold-season middle-tropospheric

86 wave cloud studies of Cooper and Vali (1981), Cotton and Field (2002), Eidhammer et al.

87 (2010) and Field et al. (2012). The prior research demonstrated that an assessment of

88 wave cloud kinematics can be used to distinguish heterogeneous from homogeneous

89 nucleation and that crystal production occurs primarily via the previously mentioned

90 freezing nucleation pathways. Further, no compelling evidence for secondary ice

91 production was reported in those prior studies.

92   Our investigation is most similar to the airborne studies of Eidhammer et al.

93 (2010) and Field et al. (2012). Those authors analyzed cold-season (late fall)

94 measurements made near, and within, wave clouds during the ICE-L project conducted in

95 2007. Their measurements were made over northern Colorado and southern Wyoming.

96 Our work is based on cold-season airborne measurements made during the Wyoming

97 Airborne Integrated Cloud Observation (WAICO) study conducted 2008 and 2009 [Wang

98 et al., 2012]. We analyze measurements made at locations where a streamline model

99 indicated our aircraft intersected air that ascended into, and descended from, wave

100 clouds. As we will discuss in detail, we develop a data set from eight flights; 80 wave

101   cloud streamlines are analyzed. In contrast, Eidhammer et al. (2010) analyzed data from

102   one flight, and modeled three streamlines. Field et al. (2012) expanded that analysis, and

103   reported on measurement/model comparisons for 28 streamlines. In their analyses, both

104   Eidhammer et al. (2010) and Field et al. (2012) exercised a streamline-following aerosol

105   and cloud microphysical parcel model, and both derived the model's initial thermal state

106   using measurements made downwind of the investigated wave clouds. In contrast, we use

107   a streamline model to track the evolution of bulk thermodynamic properties (parcel

108   microphysics is not evaluated), and we use thermodynamic measurements made

109   immediately upwind of the investigated clouds, within ascending air, to initialize the

110   model.

111
112   **2 - Measurements**

113   All measurements were acquired onboard the University of Wyoming King Air

114   [Wang et al., 2012]. The base of operations was Laramie, Wyoming. All of the sampled

115   clouds were in the altitude range 3700 to 7400 m, and were located north of Laramie,

116   within 110 km.

117   **2.1 - Temperature and Humidity**

118   Temperature (T) was measured using a reverse-flow immersion thermometer

119   [Lawson and Cooper, 1990]. Dew point temperature (T_{dp}) was derived from vapor

120   density measurements made with a LI-COR gas analyzer (model LI6262). The latter is

121   characterized by a 0.2 s time response [Dobosy et al., 1997] and this value is somewhat

122   smaller than the time response of the reverse-flow temperature sensor [~1 s; Rodi and

123   Spyers-Duran, 1972]. The inlet to the LI-COR was forward-facing and was operated

124   subisokinetically with its inlet airspeed set at approximately 18 m/s. The latter is a factor

125   of six smaller than the airspeed of the King Air (110 m/s).

126   **2.2 - Microphysics**

127   Three wing-mounted optical particle counters are used in this analysis: 1) the

128   Passive Cavity Aerosol Spectrometer Probe (PCASP), 2) the Forward Scattering

129   Spectrometer Probe (FSSP), and 3) the Two Dimensional Optical Array Probe (2DC).

130   Each of these was fabricated by Particle Measuring Systems (PMS; Boulder, CO).

131   The PCASP was used to measure the concentration of particles with diameters

132   between 0.12 µm to 3.2 µm. Particle sizing was based on laboratory calibrations

133   conducted using monodisperse test particles with refractive index $n = 1.59$ [Cai et al.,

134   2013]. PCASP concentrations were derived as the ratio of particle count rate divided by

135   a calibrated sample flow rate [Cai et al., 2013].

136   Adiabatic compression warms the aerosol stream as it approaches the PCASP

137   inlet. Strapp et al. [1992] estimated that this process occurs over 0.2 s. Once the stream

138   reaches the probe, it is warmed by three anti-ice heaters [Snider et al., 2014]. The time

139   scale for diabatic (anti-ice) heating is approximately an order of magnitude smaller than

140   the adiabatic warming. Because of both the adiabatic and diabatic processes, unactivated

141   cloud droplets (haze particles), and cloud droplets, are partially evaporated prior to sizing

142   within the PCASP. In the case of haze particles, evaporation is complete if the initial

143   particle diameter is smaller than ~1 µm [Strapp et al., 1992; Snider and Petters, 2008].

144   The FSSP was used to categorize cloud droplets sizes from 1.5 to 47.5 µm into 15

145   bins. During WAICO the cloud droplet concentrations were less than 300 cm^{-3}, so the

146   FSSP dead time and coincidence errors are less than 25 % [Baumgardner et al., 1985].

147   Both of these effects were accounted for in the data processing. Because our FSSP

148   measurements come from clouds containing ice, bias due to ice crystal shatter also needs

149   to be addressed. Since we only analyze FSSP measurements recorded near the upwind

150   edge of the clouds, where the ice crystals are small (< 100 µm) and their concentration is

151   low (< 0.4 L^{-1}), the effect of shatter on the FSSP measurements is not expected to be

152   significant [Gardiner and Hallett, 1985; Gayet et al., 1996; Field et al., 2003] and was not

153   evaluated.

154   Ice crystals were sized and counted using an optical array probe (2DC) [Pokharel

155   and Vali, 2011]. This instrument records a crystal as a two-dimensional image. Some

156   images were rejected using criteria described in Pokharel and Vali [2011]. Images which

157   passed the rejection tests were sized in the along-track direction (hereafter, this dimension

158   is termed "diameter") and these were binned into channels with lower-limit diameters set

159   at 25, 50, 100, 150, 200, 250, 300, and 400 µm for the smallest eight of 20 channels;

160   nearly all crystals recorded during WAICO classified into these eight channels. Because

161   even the largest crystals in this set are smaller than the size known to shatter when

162   impacted at aircraft velocities [Korolev and Isaac, 2005; Korolev et al., 2013], the effect

163   of shatter was ignored. Concentrations were derived by assuming that the optical depth of

164   field, for all crystals and regardless of their size, was equal to the 2DC's sampling

165   aperture (61 mm) [Vali et al., 1981]. Crystal concentration and crystal interarrival time

166   measurements, derived using the 2DC, are analyzed in greater detail in Appendix A.

167   2DC-derived concentrations were validated by Cooper and Saunders (1980). The

168   basis for their validation was airborne 2DC concentrations measured simultaneous with

169   concentrations derived by impacting ice crystals onto oil-coated slides (OCS) exposed in

170   a decelerator. Crystals impacted on the slides were photographed and counted, the counts

171   were increased by dividing by a size-dependent impaction efficiency, and diameter-

172   integrated concentrations were computed for crystals with maximum dimension larger

173   than 50 μm. The OCS concentrations were compared to 2DC concentrations. The latter

174   were derived by integrating from 50 μm to larger diameters. Cooper and Saunders

175   reported 2DC-OCS concentration ratios between 3.6 and 0.6 ($\bar{x} = 1.7$, $\sigma = 0.9$, number

176   of samples = 12). From the comparisons it was concluded that, for crystals larger than 50

177   μm, the 2DC is capable of making quantitative concentration measurements.

178   Based on the findings discussed in the previous paragraph we derived N_{IC} (Tab.

179   1) as the diameter-integrated concentration corresponding to $D > 50$ μm. Further, we

180   excluded from our analysis instances when the concentration of crystals in the first 2DC

181   channel (25 to 50 μm) exceeded more than 50 % of the overall ($D > 25$ μm) diameter-

182   integrated concentration. The intent of this criterion is avoidance of crystals whose

183   concentration is uncertain because their depth of field is ambiguous. If we had summed

184   those crystals into N_{IC}, the relative concentration bias could have approached a limiting

185   value equal to the ratio of the 2DC manufacturer's recommendation for a 25 to 50 μm

186   particle's depth of field (~4 mm) divided by the sampling aperture (61 mm) [Strapp et al.,

187   2001].

188   For both the PCASP and the 2DC, the relative Poisson sampling error was

189   evaluated as the reciprocal of the square root of particle count.

190   **2.3 – Air Motion**

191   Vertical and horizontal air velocities were derived from differential pressure

192   measurements made at the tip of the King Air's nose boom [Parish and Leon, 2013].

193   **2.4 - Lidar**

194   The upward-pointing Wyoming Cloud Lidar [Wang et al., 2009; Wang et al.,

195   2012] was used to remotely sense cloud boundaries. The lidar transmits in the near

196   ultraviolet ($\lambda = 0.355$ μm) at a pulse repetition frequency of 20 Hz. Seven lidar shots

197   were averaged, making the time between samples 0.35 s. The vertical resolution of the

198   lidar is 3.75 m. Using the lidar measurement of attenuated backscatter and depolarization,

199   we evaluated the boundaries between clear air and liquid cloud, and between liquid-

200   dominated and ice-dominated cloud (Wang and Sassen, 2001).

201   In the next section we describe our determinations of the air parcel streamlines

202   and how the lidar-derived cloud boundaries were used to evaluate the time interval, along

203   the streamlines, within the liquid-dominated portions of the clouds.

204   **3 - Analysis**

205   **3.1 - Parcel Streamlines and Parcel Thermodynamic State**

206   Here we explain how the streamlines were derived from measurements made

207   during level-flight penetrations of 35 wave clouds. In our data set we have 19

208   penetrations made along the wind, and sixteen penetrations made against the wind. Also

209   described is the parcel model we used to evaluate thermodynamic properties along the

210   streamlines.

211   An average horizontal wind speed ($\bar{u}$) was derived from airborne in-situ wind

212   measurements made during each of the cloud penetrations. That average was applied as a

213   constant in our streamline analysis. In contrast, the in-situ measured vertical wind

214   component (w) was oscillatory, so we fitted it as a sinusoid function, versus along-track

215   distance (x), and we assumed that the fitted vertical wind component ($w(x)$) did not

216   vary vertically. Fig. 1a shows the measured and fitted values of the vertical wind for a

217   penetration that we showcase to illustrate our methods.

218   Within the ascending portion of the wave structure (e.g., to the left (upwind) of x

219    $= 10.5$ km in Fig. 1a), we initialized several streamlines. The streamline center points

220   were separated by ~ 550 m along the flight track (five seconds at 110 m/s). For each of

221   the center points the 1 Hz measurements of T , T_{dp}, and pressure (P) were used to

222   derive five-second averaged values of T , T_{dp}, and P . These three properties were used

223   to fix an air parcel's initial thermodynamic state. A closed parcel model, conserving

224   potential temperature below the lifted condensation level (LCL), and equivalent potential

225   temperature, above the LCL, was used to evaluate the thermal state, along a streamline.

226   Using this model, and the aforementioned descriptions of the horizontal and vertical wind

227   components, we simulated the thermal and kinematic evolution of streamline-following

228   air parcels. One of the evaluated relationships is the parcel's temperature as a function of

229   the along-track distance. An example of this is shown in Fig. 1d. Also indicated are the

230   minimum streamline temperature (T_{low}) and the measurement of temperature (red circle)

231   made at the downwind intersection of the flight track and the streamline.

232   We compared our streamline temperatures, each evaluated at the downwind track-

233   streamline intersections, and the corresponding measured temperatures. The average

234   absolute difference is 0.3 $^{\circ}$C (number of samples $= 80$). This agreement is consistent with

235   a small effect, smaller than the temperature measurement error (±0.5 $^{\circ}$C), coming from

236   violations of either the closed parcel assumption or the assumptions of vertically-uniform

237    $w(x)$ and constant $\bar{u}$.

238

3.2 - Mixed-phase Time

239

240   The interval of time an air parcel experiences water-saturated conditions was

241   evaluated by combining the lidar measurements with the streamline information. We refer

242   to this time interval as the mixed-phase time (t_{MP}). Figs. 1b and 1c illustrate how t_{MP}

243   was evaluated. At the upwind cloud edge, at $x = 9.5$ km but above the aircraft, the

244   streamline encounters the first of two cloud boundaries. Using lidar measurements, we

245   defined this upwind cloud boundary by its increased lidar backscatter and decreased lidar

246   depolarization (compared to the depolarization in clear air). Approximately four km

247   downwind, the streamline encounters the second boundary. We defined this boundary by

248   its decreased lidar backscatter and increased depolarization. Here the boundary is

249   between liquid- and ice-dominated cloud. Further, we defined t_{MP} as the integral of the

250   parcel transit time between these two boundaries. For a few of the streamlines, the

251   downwind track-streamline intersection was within the liquid-cloud region. In those

252   cases, the calculation of t_{MP} was stopped at the intersection. The lower and upper

253   bounds of t_{MP} are 38 to 507 s; the average t_{MP} is 221 s.

254   We obtained good agreement between values of t_{MP}, based exclusively on lidar,

255   and those based partially on the in-situ measurements of T and T_{dp}. These comparisons

256   were made by differencing the lidar-derived t_{MP} and a mixed-phase time derived using

257   T - and T_{dp} -dependent determinations of the LCL (Sect. 3.1) combined with lidar-based

258   determinations of the downwind cloud boundary. In this comparison the average absolute

259   difference is 22 s. Each absolute difference was converted to a relative difference by

260   dividing by the lidar-derived values of t_{MP}. The relative differences range from 0.0 to

261   0.9.

262   **3.3 - Aerosol Particles and Cloud Droplets**

263   In this section we evaluate aerosol concentrations and compare to in-cloud droplet

264   concentrations. For each of the 35 cloud penetrations we evaluated five-second averages

265   of the PCASP and FSSP concentrations. For the PCASP, the averaging interval was

266   started five seconds upwind of the cloud, and for the FSSP, the averaging interval was

267   started at the cloud edge. Averaging intervals are shown at the bottom of Fig. 2b and at

268   the top of Fig. 2d. Also presented (Figs. 2a, 2b and 2c) are the size-resolved

269   concentrations from the PCASP, FSSP and 2DC. The series shown in Fig. 2 are for the

270   same section of flight illustrated in Fig. 1.

271   Similar to Eidhammer et al. [2010], we compared the upwind aerosol particle

272   concentration (D > 0.25 µm; five-second averaged) to the in-cloud droplet concentration

273   (D > 1.5 µm; five-second averaged). From the series presented in Fig. 2d, it can be seen

274   that droplets, measured at ~ $x = 11$ km (i.e., downwind of the cloud edge), were more

275   abundant than aerosol particles measured at ~ $x = 10.5$ km (i.e., upwind of the edge).

276   Following this same averaging procedure, we evaluated a droplet-to-aerosol ratio for 32

277   of our 35 penetrations; three of the 35 were discarded because droplets were smaller than

278   the minimum size detectable by the FSSP ($D = 1.5$ µm). In the 32 comparisons, the

279   droplet-to-aerosol concentration ratios were consistently greater than 0.7. These results

280   are consistent with the findings of Eidhammer et al. [2010]. A reasonable inference is that

281   the $D > 0.25$ µm particles are internally mixed, that the mixture's water-soluble fraction

282   promoted the nucleation of the droplets, and that the mixture's water-insoluble fraction

283   promoted ice nucleation, presumably via the condensation and immersion freezing

284   pathways. The effect of ice development on cloud properties is evident at the downwind

285   track-streamline intersection in Figs. 1 and 2. Most noticeable are the enhanced lidar

286   depolarization ratios seen at x ≥ 15 km in Fig. 1c and the enhanced diameter-integrated

287   crystal concentrations seen at x ≥ 15 km in Fig. 2d.

288   **3.4 - D > 0.5 μm Aerosol Particle and IC Concentrations**

289   In addition to the D > 0.25 μm aerosol concentrations, analyzed in the previous

290   section, we also evaluated $n_{0.5}$ (Sect. 1). These were averaged outside of cloud during

291   the five-second time windows used for thermodynamic-property averaging (Sect. 3.1).

292   For the rest of the paper, $n_{0.5}$ is reported as a particle count per standard cubic

293   centimeter (sccm^{-1}). Also for the rest of the paper, values of N_{IC} (Tab. 1) are derived as

294   five-second averages evaluated at the downwind track-streamline intersections (e.g., at ~

295   x = 15 km in Fig. 1c), and these are reported as a crystal count per standard liter (sL^{-1}).

296   **3.5 - Data Set**

297   In the previous sections we described how values of N_{IC}, $n_{0.5}$, T_{low}, and t_{MP}

298   were evaluated for each streamline. The subset $\{N_{IC}, n_{0.5}, T_{low}\}$ is the streamline data

299   we used to develop a fit of N_{IC}, according to the mathematical form of Eqn. 1.

300   However, before fitting our measurement data, we excluded streamlines affected by four

301   effects: 1) an abundance of crystals in the first 2DC channel, 2) homogeneous freezing,

302   3) crystal sublimation, and 4) variable aerosol particle and crystal concentrations.

303   Conditions for data *inclusion* are: (1) N$_{IC}$(D<50μm) must be smaller than

304   0.5·N$_{IC}$(D>25μm) (Sect. 2.2); 2) T_{low} > -35 ^{o}C [Heymsfield and Miloshevich, 1993]; 3)

14

305   ice saturated, or larger relative humidity, at the downwind track-streamline intersection;

306   and 4) relative Poisson sampling errors (Sect. 2.2) less than specified thresholds [1]. Out of

307   the 116 streamlines we analyzed, 80 satisfy our data inclusion criteria. The set

308      $\{N_{IC}, n_{0.5}, T_{low}, t_{MP}\}$ is provided for the 80 streamlines in the supplementary

309   information.

310   **4 – Fitted N_{IC} Equations**

311   In this section we show results from fitting our measurement data with both

312   temperature-dependent, and temperature-aerosol-dependent, equations. We start with a

313   solely temperature-dependent fitting equation because many previous cloud modeling

314   studies were based on such a relationship [e.g., Meyers et al., 1992], and because the rate

315   of change of crystal concentration with temperature can have a profound impact on

316   modeled cloud properties [Eidhammer et al., 2009].

317   We develop the fitting equations using logarithm-transformed crystal and

318   logarithm-transformed aerosol concentrations. The reason for log-transforming the data is

319   that we expect errors, in both crystal and aerosol concentration, to be multiplicative in the

320   sense that larger values correspond with larger error and vice versa. Multiplicative error,

321   scaling in proportion to the square root of concentration as predicted by the Poisson

322   probability law [Young, 1962; Rogers and Yau, 1989], was documented by Cai et al.

323   (2013) in their investigations of the PCASP's response to steadily-generated

324   monodisperse test particles.

---

[1] The relative Poisson error thresholds adopted for IC concentration and for $n_{0.5}$, were 0.4 and 0.7, respectively. These values cut the distributions of the relative Poisson errors at their 99th percentiles.

325   Fig. 3a shows the temperature-dependent fit (i.e., $N_{IC}(T_{low})$) plotted versus

326   measured N_{IC}. The square of the Pearson correlation coefficient (r^2), for this scatter

327   plot, is relatively small and demonstrates that temperature alone, via the fit equation, can

328   only explain 51% of the N_{IC} variability.

329   In Fig. 3b we plot our fitted values of $N_{IC}(T_{low}, n_{0.5})$ versus measured N_{IC}.

330   Results shown here are for one of two fitting methods we implemented. In fit method #1

331   we used the Matlab Curve Fitting Toolbox (The MathWorks, Natick, MA), with the log-

332   transformed version of Eqn. 1, and derived the logarithm of a ($ln\, a$), and the values of

333   b, c and d. We also fitted the set $\{N_{IC}, n_{0.5}, T_{low}\}$ using the using the three-step

334   procedure described in D10. We refer to the latter as method #2 and describe our

335   implementation of that method in Appendix B. The advantage of method #1 is that it

336   shortens D10's three-step procedure to one step.

337   The fit coefficients derived by D10, our fit coefficients (methods #1 and #2), and

338   the method #1 and #2 statistical errors, expressed as standard deviations, are presented in

339   Tab. 2. Focusing on results obtained using method #1, our four coefficients are seen to

340   agree within two standard deviations of D10's. Also, agreement within two standard

341   deviations was obtained between our application of method #2 and D10's.

342   By inputting the statistical errors from Tab. 2 into a propagation of error equation

343   (Young, 1962; their Eqn. 13.9), we evaluated contributions to the relative variance of the

344   logarithm of $N_{IC}(T_{low}, n_{0.5})$ (method #1). For $n_{0.5} \leq 3.4$ sccm^{-1} (the average for our

345   data set), and for temperatures over the full range of our data set ($-34 \leq T_{low} \leq -14\ ^{\circ}$C),

346   the relative variance is controlled by terms proportional to both the square of the

347   statistical error in $\ln a$ and the square of the statistical error in b. Further, we also

348   evaluated the fractional standard deviation of $N_{IC}(T_{low}, n_{0.5})$ (method #1). For the same

349    $n_{0.5}$ and T_{low} settings provided above, the fractional standard deviation is ~ 4 and

350   increases to ~ 5 if $n_{0.5}$ is set to 16 sccm^{-1} (the maximum for our data set). Yet, in spite of

351   this uncertainty, our fitted (method #1) and measured values are seen to correlate over IC

352   concentrations that range from 0.1 to 100 sL^{-1} (Fig. 3b). Also illustrated are fitted

353   concentrations, derived using Eqn. 1 with D10's coefficients, and our measurements of

354   T_{low} and $n_{0.5}$. In either case the r^2 is ~ 0.7 and thus larger than that for the

355   temperature-only fit (cf., Fig. 3a).

356   We also evaluated the fraction of the measured crystal concentrations that plot

357   within a factor of two of the fit. Based on our method #1 coefficients, this percentage is

358   69% and thus larger than the percentage (66 %) based on fit coefficients from D10 (the

359   percentage is 71% when using the method #2 coefficients; not shown here). Thus, we

360   obtained better fitted-vs.-measured agreement with our method #1 and method #2 fit

361   coefficients and somewhat poorer agreement with the D10 coefficients.

362   **5 – Effect of Mixed-phase Time**

363   As was discussed in the introduction, there is an outstanding question in

364   atmospheric science community regarding the time-dependent nature of ice nucleation.

365   Of relevance for our data set, with its average $t_{MP} = 221$ s (Sect. 3.2), is the possibility that

366   the characteristic time for an embryo to transition to a crystal is comparable to t_{MP}. If that

367   were the case, we would expect that streamlines associated with larger mixed-phase

368   times, all other things equal, would have larger IC concentrations. The work of Vali and

17

369   Snider (2014) provides an estimate the effect. They show that time dependency can alter

370   crystal concentrations by up to a factor of three depending on whether a time- and

371   temperature-dependent parameterization or purely temperature-dependent

372   parameterization is used to describe heterogeneous ice nucleation.

373   We investigated time dependency by stratifying our 80 determinations of $\{N_{IC},$

374    $n_{0.5}, T_{low}, t_{MP}\}$ into four T_{low} subsets. In Tab. 3 we present the subset's minimum and

375   maximum temperatures, the averaged $n_{0.5}$, and the number of data values. For each of

376   these we tested the hypothesis that $ln(N_{IC})$ is correlated with $ln(t_{MP})$. Values of the

377   Pearson correlation coefficients (r), and the levels of significance (p), demonstrate that

378   none of the correlations are significant (i.e., all have $p > 0.05$). This same conclusion was

379   reached after removing from the correlations those points exhibiting the largest t_{MP}

380   uncertainty (relative difference > 0.3, Sect. 3.2), but those results are not shown in Tab. 3.

381   We also stratified by $n_{0.5}$ within the four T_{low} subsets. One of those correlations

382   ($ln(N_{IC})$ versus $ln(t_{MP})$) approaches statistical significance, with $p = 0.1$ and with 10

383   paired values; the rest have $p > 0.1$. That subset plots in the gray rectangle shown in Fig.

384   4a and the N_{IC} versus t_{MP} correlation for that subset is shown in Fig. 4b.

385   In spite of these suggestions of a connection between crystal concentration and

386   mixed-phase time we cannot argue convincingly that time-dependent effects were

387   significant for crystals within the clouds we studied. Our ability to argue for, or against a

388   dependence on t_{MP}, was limited by the strong temperature-dependence of ice nucleation.

389   This is evident from Fig. 3a where the value $k_2 = 0.22\ ^oC^{-1}$ cat be used to demonstrate that

390   a 5 ^oC decrease corresponds to a factor of three increase in nucleated concentration. Also

18

391   limiting is the relatively few data values within our 5 ^{o}C subsets. Thus, in future wave

392   cloud studies, attention should be paid to strategies which generate an adequate number

393   of points within specified temperature and aerosol ranges.

394   **6 – Summary and Conclusion**

395   The result we present in Tab. 2, with fit coefficients generally consistent, in a

396   statistical sense, with those reported by D10, is important because it validates D10's

397   approach using different methodology. In short, we use a streamline model to connect a

398   measurement of aerosol concentration ($n_{0.5}$), made upwind of a wave cloud, to a

399   downwind measurement of IC concentration. Our reconfirmation of the relationship

400   between crystals and $n_{0.5}$, implied by Eqn. 1, is conceptually appealing because it

401   acknowledges that aerosol particles are necessary for the occurrence of heterogeneous ice

402   nucleation. Appeal also comes from the linkage provided by Eqn. 1, through aerosol, to

403   cloud processes.

404   We also probed the conjecture that the duration of ice nuclei exposure to water-

405   saturated conditions is a determinant of IC concentration. Our analysis shows no

406   statistically-robust evidence for this. This finding is relevant to descriptions of ice

407   nucleation within water-saturated layer clouds (e.g., stratocumulus and altostratus) where

408   temperature is relatively uniform, and steady, and where time-dependent ice nucleation is

409   suspected of occurring continuously and with substantial meteorological impact [Crosier

410   et al., 2011; Westbrook and Illingworth, 2013]. In fact, many model representations of

411   heterogeneous nucleation anticipate this time-dependent, constant-temperature,

412   phenomenon. Also, in some models, the nucleation rate is set to zero when the

413   temperature tendency is zero or positive [Khain et al., 2000; Muhlbauer and Lohmann,

414   2009], but this action is not supported by all of the experimental evidence currently

415   available (for a review, see Vali (2014)). Further investigation is needed to confirm our

416   conclusion of little, if any, time-dependent effect within the cloud type we studied

417   (middle-tropospheric wave clouds). Going forward, we anticipate our methodology will

418   help advance understanding of time-dependent atmospheric ice nucleation, and

419   atmospheric ice nucleation in general.

420

421   **Appendix A**

422   In this appendix we examine the reliability of ice crystal concentrations derived

423   using the University of Wyoming 2DC. We derive concentrations using the Wyoming

424   2DC, with its slower-responding photodiode array (Gayet et al., 1993; Baumgardner and

425   Korolev, 1997; Strapp et al., 2001), and compare to values derived using a faster

426   responding cloud imaging probe (CIP; Baumgardner et al., 2001). We also analyze the

427   2DC ice crystal interarrival times and investigate crystal shattering. Two data sets are

428   analyzed. The first comes from Wyoming King Air flight data, acquired on 9 January

429   2011 during the Colorado Airborne Multi-Phase Cloud Study (CAMPS), and the second

430   comes from the 80 downwind track-streamline intersections described in Sect. 3.5. Both

431   the 2DC and CIP were operated with standard probe tips (Korolev et al., 2013).

432   Strapp et al. (2001) conducted laboratory studies that investigated a 2DC's ability

433   to detect objects (circular dots) positioned away from the center of focus of the probe's

434   laser. They demonstrated that the probe's finite response led to undersizing, counting

435   losses and image distortion.   At dot sizes smaller than 100 μm, undersizing and counting

436   losses increased with the speed the dots transited through the probe's sample volume.

437   Strapp et al. conducted their testing using dots deposited onto a glass disk. The dots were

438   opaque, monodisperse, and regularly spaced on the disk along circular tracks. The disk

439   was positioned with its rotational axis parallel to the 2DC laser beam. The position of the

440   disk plane, relative to the center of focus of the beam, was varied. The largest dot speeds

441   tested by Strapp et al. were comparable to the airspeed of the Wyoming King Air (~100

442   m/s).

443

A1 - 2DC and CIP Concentrations

444

445   A comparison of 2DC- and CIP-derived concentrations was made using Wyoming

446 King Air data acquired on 9 January, 2011 (20110109). The comparison data was selected

447 from three level-flight transits of an orographic cloud. The cloud was located over

448 continental divide in northern Colorado. During the cloud transits the liquid water content

449 was less than 0.2 g m^{-3} and temperature was between -23 and -25 ^{o}C. We processed the

450 raw 2DC and CIP measurements the same way we processed the WAICO 2DC

451 measurements (Sect. 2.2). Also consistent with the WAICO processing, the compared

452 concentrations are five-second averages and are for crystals larger than 50 µm (sized

453 along the aircraft track). The CIP/2DC comparison is shown in Fig. A1a. The vertical line

454 at 5 L^{-1} marks the median of the 80 concentrations in our WAICO data set (Sect. 3.5), and

455 its implication is discussed in the following paragraph.

456   Because of the undersizing and counting losses documented for a 2DC, especially

457 at the low end of its range (D < 100 µm), and the fact these effects are attributed to the

458 relatively slow time response of the 2DC's optical array (Strapp et al., 2001), we expected

459 that concentrations derived using the faster responding CIP (Baumgardner et al., 2001)

460 would exceed 2DC-derived values. Contrary to that expectation, we found reasonable

461 agreement (Fig. A1a). Measures of the agreement are as follows: 1) For concentrations

462 larger than 5 sL^{-1}, all of the 2DC-derived values plot well within a factor of two of the

463 CIP. 2) For concentrations smaller than 5 sL^{-1}, a large fraction of the 2DC values (87%)

464 plot within a factor of two of the CIP. These findings, combined with the findings of

465 Cooper and Saunders (1980) (also see Sect. 2.2), lend confidence to the concentration

466 values we derived using 2DC measurements made during WAICO. However, this

467 comparison does not completely lessen the concern that we biased the WAICO

468 concentrations at $D < 100$ μm by assuming that the 2DC's optical depth of field was

469 independent of crystal size and equal to the probes's sampling aperture (61 mm) (Vali et

470 al., 1981 and Sect. 2.2).

471 **A2 - Interarrival Time and Shattering**

472   Representative CIP and 2DC size distributions, from CAMPS, are shown in Fig.

473 A1b. It is evident that most of the detected crystals are smaller than 400 μm, especially in

474 the 2DC measurement. A size distribution from one of the 80 WAICO downwind track-

475 streamline intersections is shown in Fig. A2a. The largest crystal detected in this five-

476 second interval is 400 μm. A histogram of crystal interarrival times for the same five-

477 second interval is shown in Fig. A2b. Evident in the left tail of the histogram is a

478 minimum, at interarrival time $\tau^* = 2\text{x}10^{-3}$ s, where we delineate between a fragment

479 mode ($t < \tau^*$) and a mode corresponding to intact crystals ($t > \tau^*$). We note that only 7%

480 of the crystal counts classify as fragments and that this fraction is much smaller than the

481 example presented by Korolev et al. (2013) for a 2DC with standard probe tips (their Fig.

482 14a).

483   We analyzed interarrival times obtained from each of the 80 WAICO downwind

484 track-streamline intersections. Histograms were binned as in A2b (3.5 bins per decade)

485 and all particle images, including those that did not pass the rejection criteria of Pokharel

486 and Vali (2011) (Sect. 2.2), were used. We developed a procedure that searches the

487 histogram for a minimum between $t = 10^{-6}$ s and the histogram mode. In our set of 80

488 there are 16 cases that do not exhibit a minimum and 21 with a provisionally significant

489 minimum. The provisional cases were characterized by a cumulative fraction, evaluated

490   at the minimum, greater than 20%. The example shown in Fig. A2b is not a provisional

491   case because the cumulative fraction at $\tau^* = 2\text{x}10^{-3}$ s is less than 20%. All of the

492   provisional cases exhibited a minimum that was within an order of magnitude of the

493   histogram mode. Because order-of-magnitude separation is substantially less than the

494   minimum-to-mode separation seen Korolev et al. (2013) (their Fig. 14), we concluded

495   that a fragment mode could not be discerned. Thus, we ignored the effect of shattering.

496   Twenty six of the remaining 43 cases (43=80-16-21) had a minimum more than an order

497   of magnitude smaller than the histogram mode; Fig. A2b is an example. For these we

498   ignored the effect of shattering because the fraction affected was less than 20% and

499   because the rejection criteria of Pokharel and Vali (2011) removes some of the affected

500   crystals from the population used to evaluate the concentration.
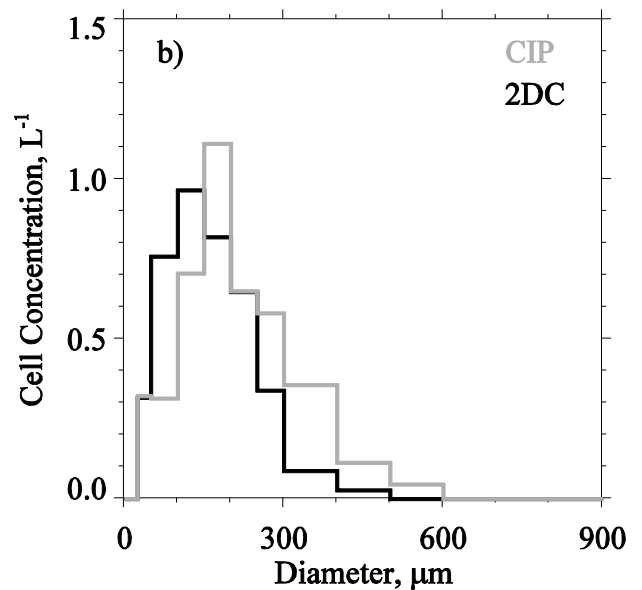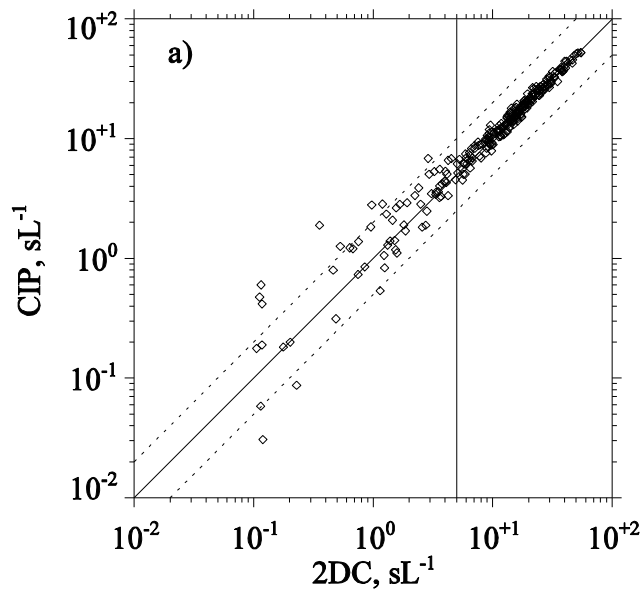
501

502

503

504

505

506

507

508

509

510

511

512

513   Fig. A1 – a) The CIP/2DC concentration comparison. Compared values are five-

514 second averages and are for crystals larger than 50 μm. Comparison data is from

515 20110109 during the Colorado Airborne Multi-Phase Cloud Study (CAMPS). Wyoming

516 King Air data shown here was selected from three along-wind level-flight cloud transits:

517 1) 221200 to 222200 UTC, 2) 223900 to 224800 UTC, and 3) 230600 to 231600 UTC.

518 The vertical line at 5 sL^{-1} is drawn at the median value for our set of 80 WAICO 2DC-

519 derived measurements. b) 2DC and CIP size distributions from a representative five-

520 second subset (224646 to 224650 UTC) of the flight on 20110109.

521

522
523
524
525
526
527
528
529
530

531
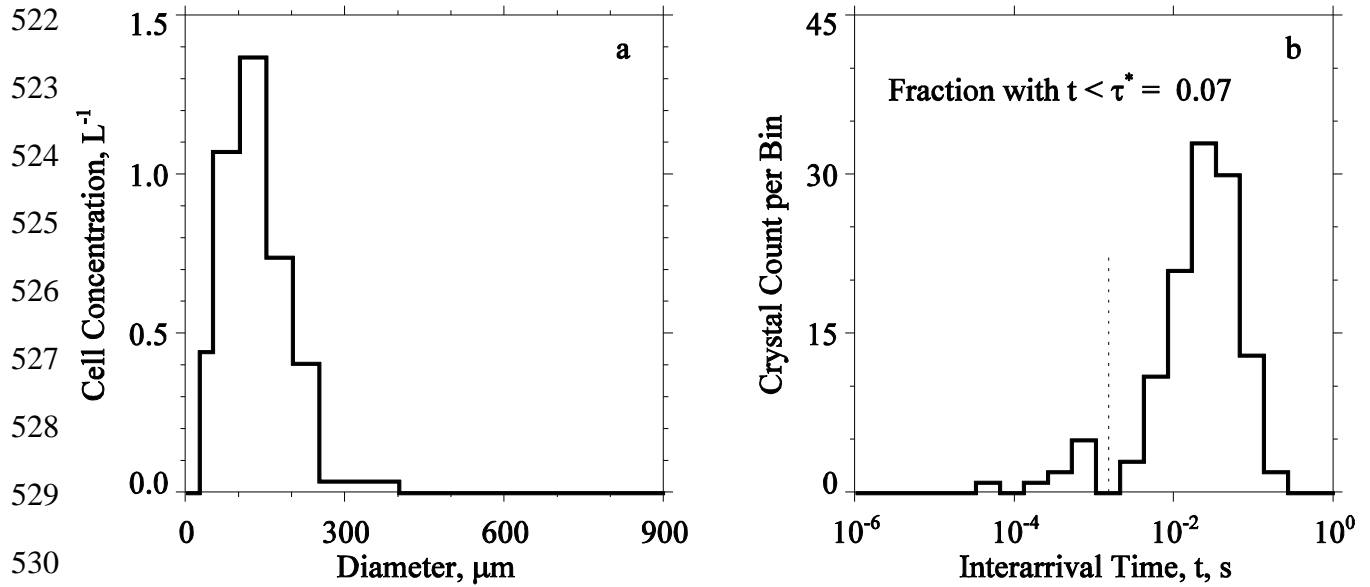
Fig. A2 – a) The 2DC size distribution derived for the WAICO 181933 to 181937

interval on 20080227. This interval corresponds to the downwind track-streamline

intersection at x=15 km in Fig. 1c. b) The interarrival time histogram for the 181933 to

181937 interval on 20080227. The vertical dashed line marks a minimum between a

fragment mode ($t < \tau^*$) and a mode corresponding to intact crystals ($t > \tau^*$).

537

538   **Appendix B**

539
540   Here we describe how we fitted our 80 determinations of the set

541     $\{N_{IC}, n_{0.5}, T_{low}\}$ using the three step procedure developed by D10 (herein method #2).

542   In the first step, the data were binned into four $(273.16 - T_{low})$ subsets; the number of

543   samples in the four subsets is provided in Table 3. In the second step, values of $ln(p_i)$

544   and q_i were derived for each subset by regression. Here "i" indicates the temperature

545   subset and the form of the regression equation is

546             $$ln(N_{IN,i}) = ln(p_i) + q_i \cdot ln(n_{0.5,i}).$$ (B1)

547   In the third step, the values of $ln(p_i)$ were regressed vs. $ln(273.16 - T_{low,i})$, and

548   also, the values of q_i were regressed vs. $T_{low,i}$. In these regressions the $T_{low,i}$ is the

549   average of the subset. The slopes and intercepts of these regressions define the method #2

550   coefficients $ln(a)$, b, c and d

551             $$ln(a) = \text{intercept}\left(ln(p_i) \text{ vs. } ln(273.16 - T_{low,i})\right)$$ (B2)

552             $$b = \text{slope}\left(ln(p_i) \text{ vs. } ln(273.16 - T_{low,i})\right)$$ (B3)

553             $$c = \text{slope}\left(q_i \text{ vs. } (273.16 - T_{low,i})\right)$$ (B4)

554             $$d = \text{intercept}\left(q_i \text{ vs. } (273.16 - T_{low,i})\right).$$ (B5)

555

562
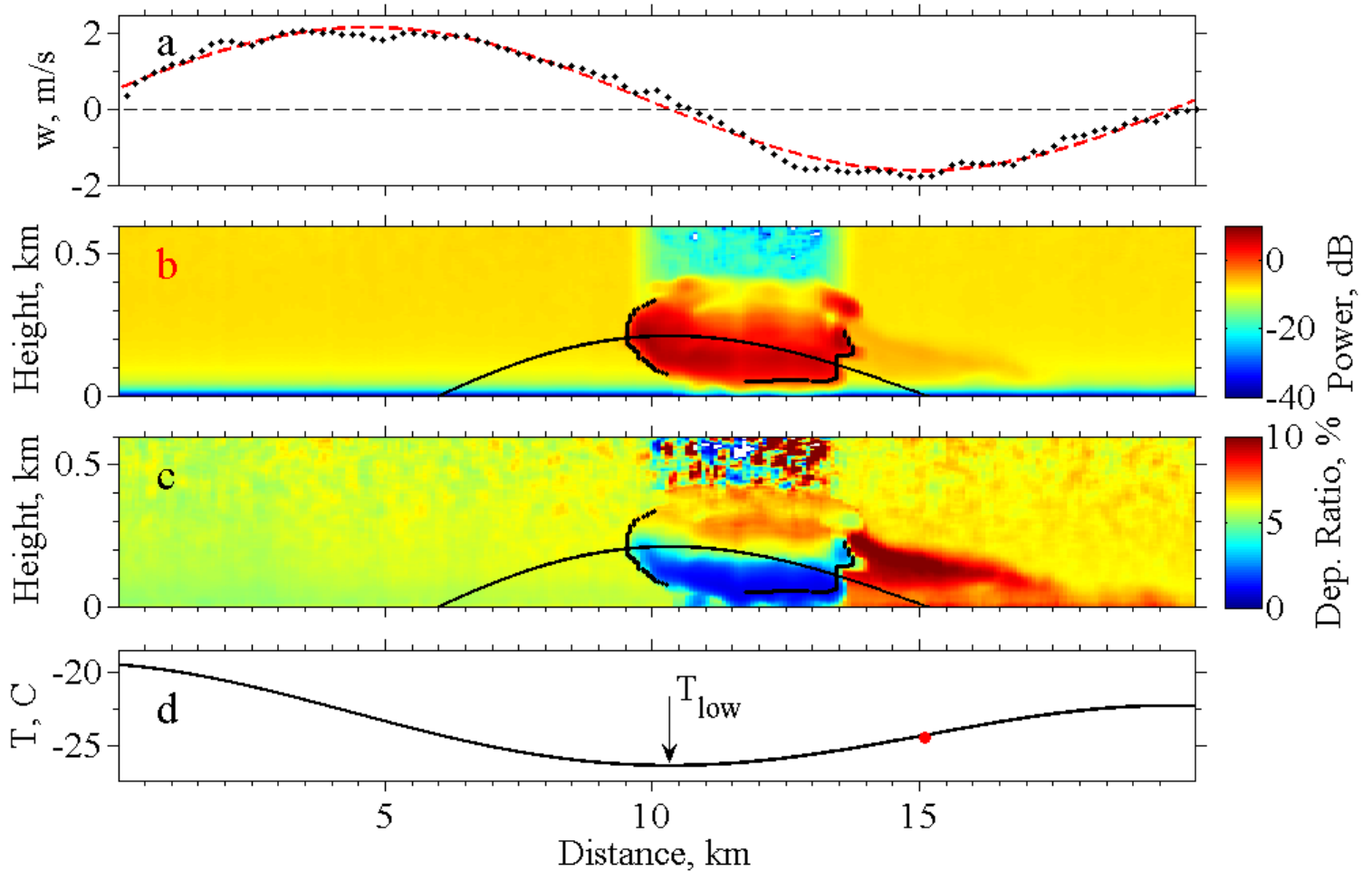
574   Fig. 1. Level-flight sampling a few tens of meter below a wave cloud between

575   18:17:45 and 18:20:09 on February 27, 2008. Airflow is from left to right. (a) In-situ

576   vertical velocity measurements and the sinusoid fit. (b) The example streamline (black)

577   overlain on lidar backscattered power; the two other black lines delineate the liquid-cloud

578   and ice-cloud boundaries discussed in the text. (c) Example streamline overlain on lidar

579   depolarization ratio; the two other black lines delineate the liquid-cloud and ice-cloud

580   boundaries discussed in the text. d) Streamline temperature, minimum streamline

581 temperature, and the in-situ measured temperature at the downwind track-streamline

582 intersection (red circle).

583
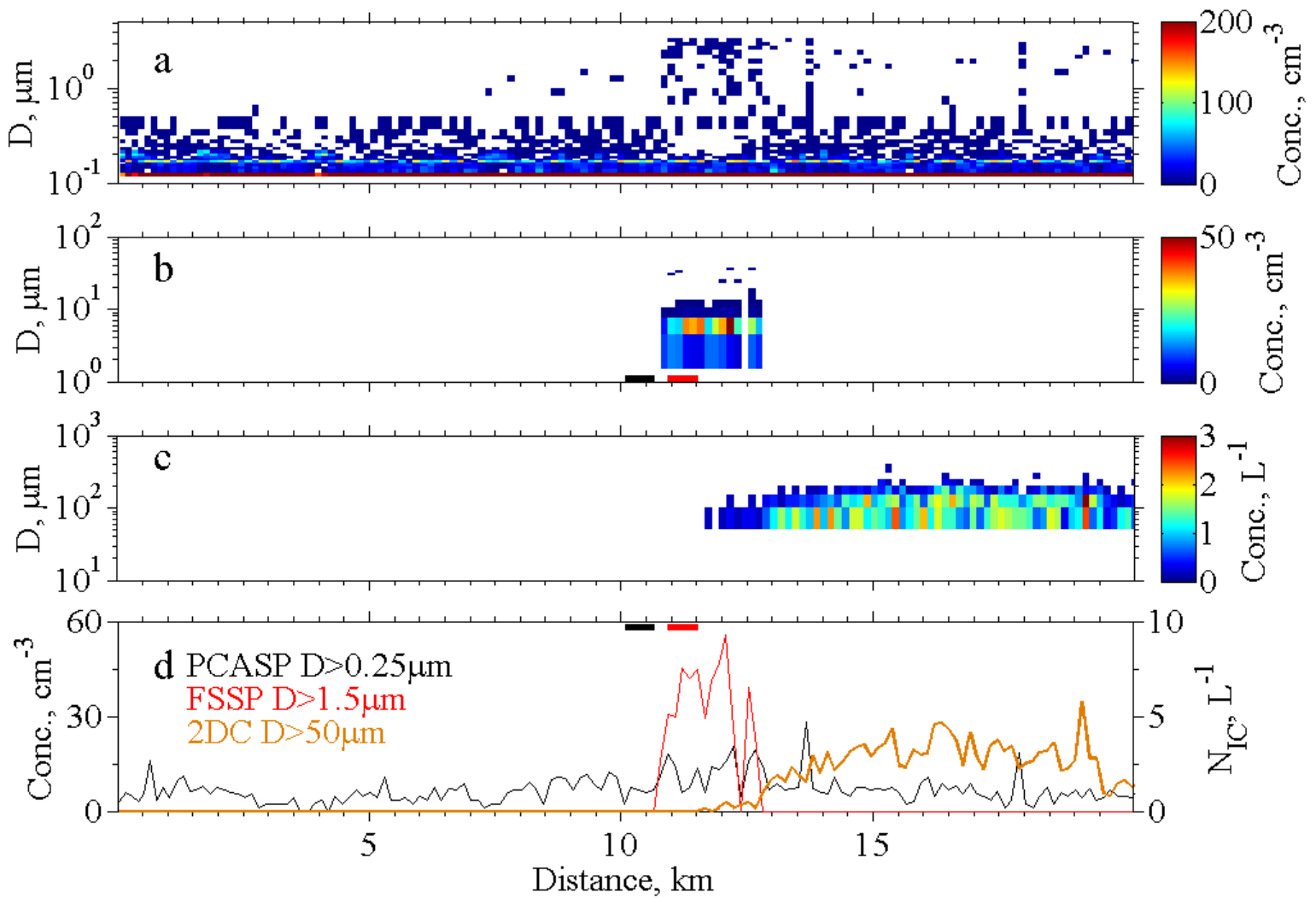
596   Fig. 2. The same segment of flight as shown in Fig. 1. (a) Size-resolved PCASP

597   concentrations. (b) Size-resolved FSSP concentrations. The black and red horizontal

598   rectangles at the bottom of this panel are the five-second averaging intervals for aerosol

599   and droplets analyzed in Sect. 3.3. (c) Size-resolved 2DC concentrations. (d) Diameter-

600   integrated PCASP (D > 0.25 µm, black line), diameter-integrated FSSP (D > 1.5 µm, red

601   line), and diameter-integrated 2DC (D > 50 µm, orange line) concentrations. Averaging

602   intervals for aerosol and droplets are repeated from panel b.

603   31
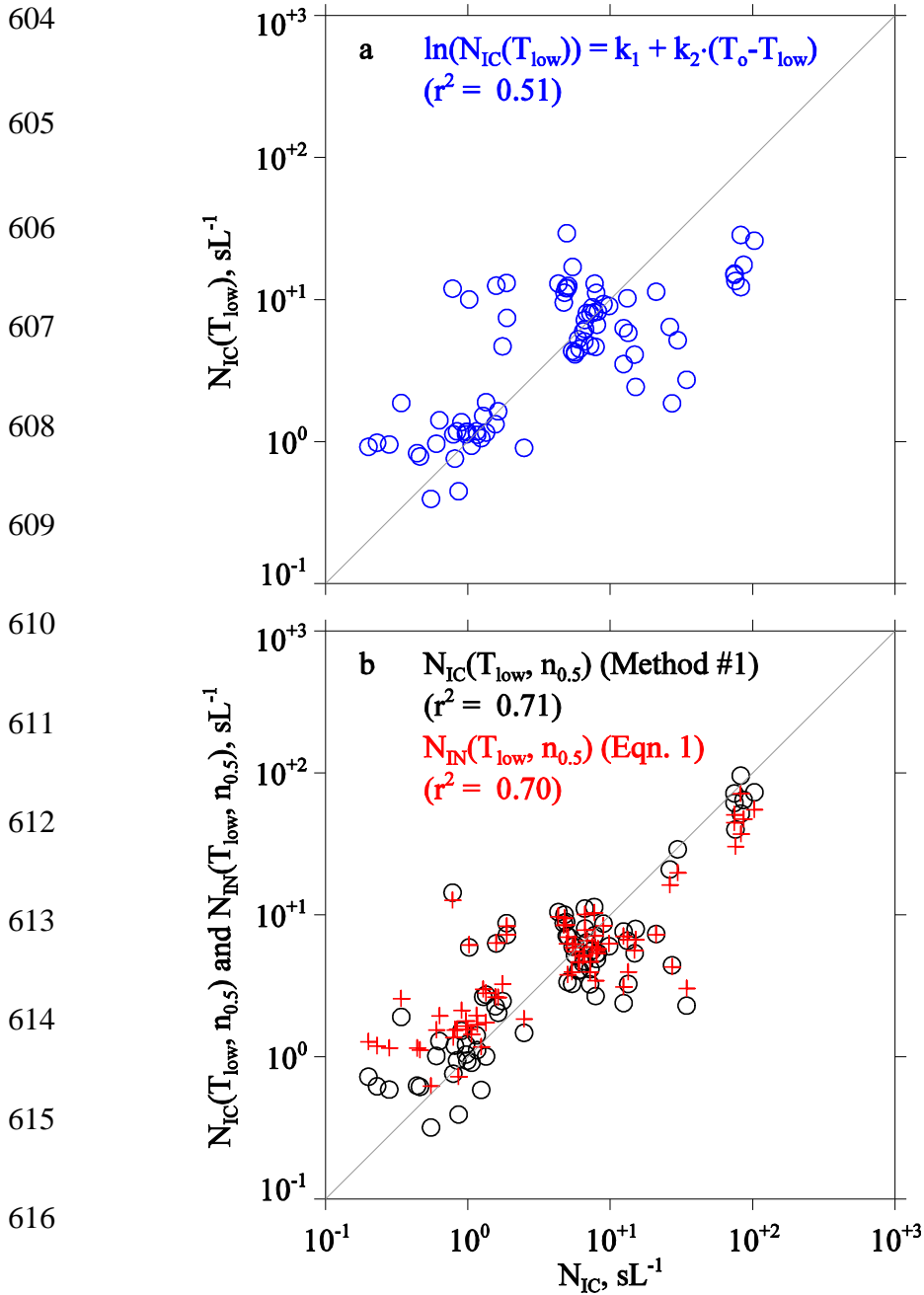
Fig. 3. a) Values of $N_{IC}(T_{low})$ ($\ln(N_{IC}(T_{low})) = k_1 + k_2 \cdot (T_o - T_{low})$ with $k_1 = -4.04$

and $k_2 = 0.22\ ^{\circ}C^{-1}$) plotted versus measured N_{IC}. b) As in Fig. 3a, but with

$N_{IC}(T_{low}, n_{0.5})$ (method #1 fit coefficients), and $N_{IN}(T_{low}, n_{0.5})$ (Eqn. 1), plotted

versus measured N_{IC}. In Figs. 3a and Fig. 3b, the square of the Pearson correlation

622   coefficients (r^2) was evaluated using log-transformed concentrations. Also, the one-to-

623   one line is shown in both panels.

624

625

626

627

628

629

630

631

632

633

634

635

636

637

638

639

640

641

Panel a axis labels: D > 0.5 μm Concentration, $n_{0.5}$, sccm^{-1} (y-axis); Minimum Streamline Temperature, T_{low}, °C (x-axis). y-axis ticks: 0, 6, 12, 18. x-axis ticks: -34, -24, -14.

Panel b:
Fitted Eqn.: $\ln(N_{IC}) = c_1 + c_2 \cdot \ln(t_{MP})$
$c_1 = -2.79$
$c_2 = 0.41$
$r = 0.36$
$p = 0.1$
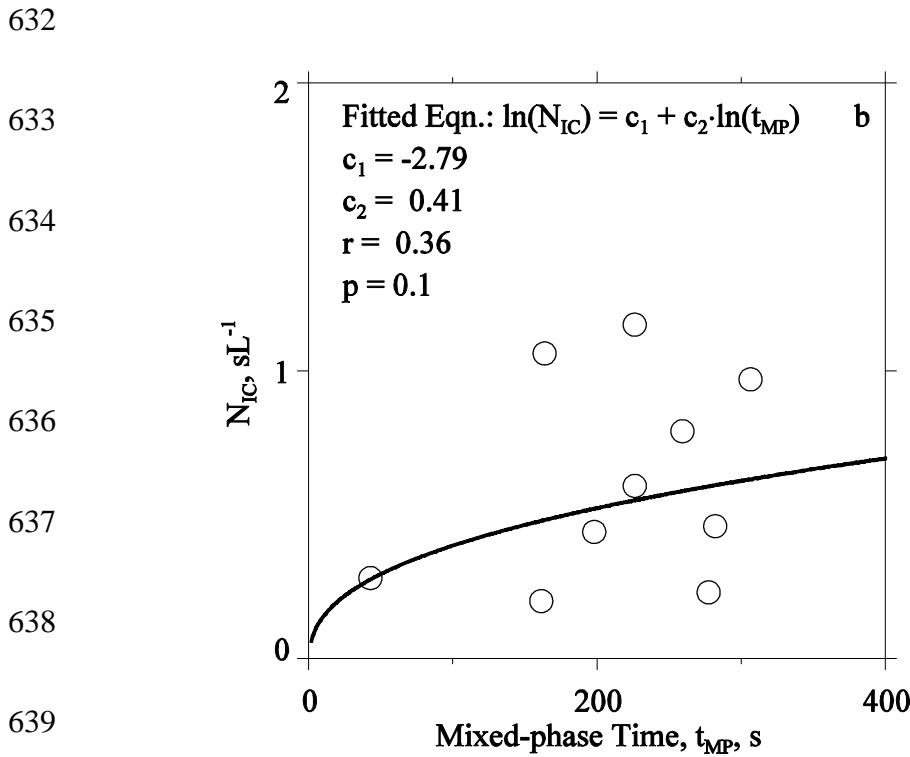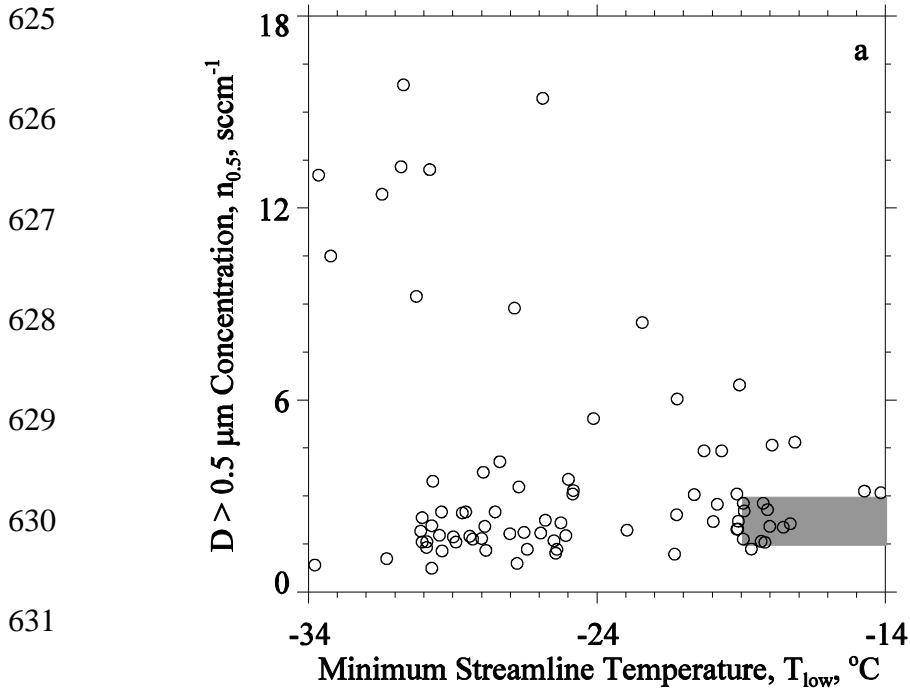
Panel b axis labels: N_{IC}, sL^{-1} (y-axis); Mixed-phase Time, t_{MP}, s (x-axis). y-axis ticks: 0, 1, 2. x-axis ticks: 0, 200, 400.

Fig. 4 - a) The 80 paired values of $n_{0.5}$ and t_{MP} in our data set. The gray

rectangle highlights the 10 points in the subset defined by -19 ≤ T_{low} < -14 °C and 1.5 ≤

34

642   $n_{0.5} < 3.0$ sccm^{-1}. b) The 10 paired values of N_{IC} and t_{MP} from the gray rectangle

643   shown in Fig. 4a. The black line is the fitting equation $ln(N_{IC}) = c_1 + c_2 \cdot ln(t_{MP})$. The

644   Pearson correlation coefficients (r), and the level of significance (p), were evaluated

645   using the log-transformed concentrations and log-transformed mixed-phase times.

646

647

648   Tab. 1 - Symbols used to represent aerosol, IN and IC concentrations
649

Symbol	Definition	Dimension
$n_{0.5}$	Measured aerosol concentration ($D > 0.5$ µm)	sccm^{-1} [a]
N_{IC}	Measured IC concentration ($D > 50$ µm) [b]	sL^{-1} [c]
$N_{IC}(T)$	Temperature-dependent fit of IC concentration (see Sect. 4)	sL^{-1}
$N_{IC}(T, n_{0.5})$	Temperature- and aerosol-dependent fit of IC concentration (see Sect. 4)	sL^{-1}
$N_{IN}(T, n_{0.5})$	Temperature- and aerosol-dependent fit of IN concentration (D10) (see Eqn. 1)	sL^{-1}

650

651   [a] Aerosol particle count per standard cubic centimeter at P=1.013x10^5 Pa and T=273.15 K

652   [b] 2DC concentration for crystals sizing larger than 50 µm (see Sect. 2.2)

653   [c] Particle count per standard liter at P=1.013x10^5 Pa and T=273.15 K

654

655   Tab. 2 - Eqn. 1 fit coefficients

Coefficients	Fit D10 [a]	Fit Method #1	Statistical Error Method #1 [b]	Fit Method #2	Statistical Error Method #2 [c]
$ln\,a$	-9.73	-15.26	2.87	-15.03	4.11
b	3.33	4.94	0.88	4.86	1.30
c	0.0264	0.0028	0.0308	0.0038	0.034
d	0.0033	0.86	0.88	0.82	0.83

656

657   [a] Fit coefficients from D10

658   [b] The standard deviations for coefficients fitted via method #1

659   [c] The standard deviations for coefficients fitted via method #2

662

663

664   Tab. 3 - T_{low} subsets and the $ln(N_{IC})$ vs. $ln(t_{MP})$ correlations

T_{min}	T_{max}	$\overline{n_{0.5}}$	Number of samples	r [a]	p [b]
-34	-29	5.50	20	0.20	0.20
-29	-24	2.93	30	0.21	0.14
-24	-19	3.50	15	-0.05	0.57
-19	-14	2.57	15	0.06	0.44

665

666   [a] The Pearson correlation coefficient for the regression of $ln(N_{IC})$ versus $ln(t_{MP})$

667   [b] Level of significance, values of this parameter greater than $p = 0.05$ indicate an
668   insignificant correlation

669

670 **8 - References**

671   Baumgardner, D., W. Strapp and J.E. Dye, Evaluation of the forward scattering

672 spectrometer probe. Part II: Corrections for coincidence and dead-time losses, *J. Atmos.*

673 *Oceanic Tech.*, 2, 626-632, 1985

674   Baumgardner, D., and A.Korolev, Airspeed corrections for optical array probe

675 sample volumes, J. Atmos. Oceanic Technol., 14, 1224-1229, 1997

676   Baumgardner, D., H.Jonsson, W.Dawson, D.O'Connor and R.Newton, The cloud,

677 aerosol and precipitation spectrometer: a new instrument for cloud investigations, Atmos.

678 Res., 59-60, 251-264, 2001

679   Bigg, E.K., The supercooling of water, *Proc. Phys. Soc. B.*, 66, 688–694, 1953

680   Braham, R.R. and P.Squires, Cloud Physics-1974, *Bull. Amer. Meteor. Soc.*, 55,

681 543–586, 1974

682   Cai, Y., J.R. Snider, and P. Wechsler, Calibration of the passive cavity aerosol

683 spectrometer probe for airborne determination of the size distribution, *Atmos. Meas.*

684 *Tech.*, 6, 2349-2358, 2013

685   Cantrell, W., and A. Heymsfield, Production of ice in tropospheric clouds: A

686 review. *Bull. Amer. Meteor. Soc.*, 86, 795–807, 2005

687   Cooper, W.A. and C.P.R.Saunders, Winter storms over the San Juan Mountains.

688 Part II: Microphysical processes, *J. Appl. Meteor.*, 19, 927–941, 1980

689   Cooper, W.A., and G. Vali, The origin of ice in mountain cap clouds, *J. Atmos.*

690 *Sci.*, *38*, 1244-1259, 1981

691   Crosier, J., K.N. Bower, T.W. Choularton, C.D. Westbrook, P.J. Connolly, Z.Q.

692 Cui, I.P. Crawford, G.L. Capes, H. Coe, J.R. Dorsey, P.I. Williams, A.J. Illingworth, M.W.

693   Gallagher and A.M. Blyth, Observations of ice multiplication in a weakly convective cell

694   embedded in supercooled mid-level stratus, *Atmos. Chem. Phys.*, 11, 257-273, 2011

695   Cotton, R. and P. Field, Ice nucleation characteristics of an isolated wave cloud,

696   *Q. J. Roy. Meteor. Soc.*, 128, 2417-2437, 2002

697   DeMott, P.J., A.J. Prenni, X. Liu, S.M. Kreidenweis, M.D. Petters, C.H. Twohy,

698   M.S. Richardson, T. Eidhammer and D.C. Rogers, Predicting global atmospheric ice

699   nuclei distributions and their impacts on climate, *P. Natl. Acad. Sci.*, 107, 11217-11222,

700   2010

701   DeMott, P.J., A.J. Prenni, G.R.McMeeking, R.C.Sullivan, M.D.Petters, Y.Toba,

702   M.Niemand, O.Möhler, J.R.Snider, Z.Wang and S.M. Kreidenweis, Integrating laboratory

703   and field data to quantify the immersion freezing ice nucleation activity of mineral dust

704   particles, *Atmos. Chem. Phys. Discuss.*, 14, 17359-17400, 2014

705   Dobosy, R.J., T.L. Crawford, J.I. MacPherson, R.L. Desjardins, R.D. Kelly, S.P.

706   Oncley and D.H. Lenschow, Intercomparison among four flux aircraft at BOREAS in

707   1994, *J. Geophys. Res.-Atmos.*, 102, 29101-29111, 1997

708   Eidhammer, T., P.J. DeMott and S.M. Kreidenweis, A comparison of

709   heterogeneous ice nucleation parameterizations using a parcel model framework, *J. of

710   Geophys. Res.*, 114, D06202, 2009

711   Eidhammer, T., P. J. DeMott, A. J. Prenni, M. D. Petters, C. H. Twohy, D. C.

712   Rogers, J. Stith, A. Heymsfield, Z. Wang, K. A. Pratt, K. A. Prather, S. M. Murphy, J. H.

713   Seinfeld, R. Subramanian, and S. M. Kreidenweis, Ice initiation by aerosol particles:

714   Measured and predicted ice nuclei concentrations versus measured ice crystal

715   concentrations in an orographic wave cloud, *J. Atmos. Sci.*, 67, 2417-2436, 2010

716   Field, P.R., R.Wood, P.R.A.Brown, P.H.Kaye, E.Hirst, R.Greenaway and J.A.

717 Smith, Ice particle interarrival times measured with a fast FSSP, *J. Atmos. Oceanic Tech.*,

718 20, 249-261, 2003

719   Field, P.R., A.J. Heymsfield, B.J. Shipway, P.J. DeMott, K.A. Pratt, D.C. Rogers,

720 J. Stith and K.A. Prather, Ice in clouds experiment-layer clouds. Part II: Testing

721 characteristics of heterogeneous ice formation in lee wave clouds, *J. Atmos. Sci.*, 69,

722 1066-1079, 2012

723   Gardiner, B.A. and J. Hallett, Degradation of in-cloud forward scattering

724 spectrometer probe measurements in the presence of ice particles, *J. Atmos. Oceanic*

725 *Tech.,* 2, 171-180, 1985

726   Gayet, J.F., P.R.A. Brown, and F.Albers, A Comparison of In-Cloud

727 Measurements Obtained with Six PMS 2D-C Probes. J. Atmos. Oceanic Technol., 10,

728 180–194, 1993

729   Gayet, J. F., G. Febvre, and H. Larsen, The reliability of the PMS FSSP in the

730 presence of small tee crystals, *J. Atmos. Oceanic Tech.*, 13, 1300-1310, 1996

731   Hoose, C., J.E.Kristjánsson, J.-P. Chen and A. Hazra, A classical-theory-based

732 parameterization of heterogeneous ice nucleation by mineral dust, soot and biological

733 particles in a global climate model, *J.Atmos.Sci.*, 67, 2483-2503, 2010

734   Heymsfield, A.J. and D.Baumgardner, Summary of a workshop on processing of

735 2D probe data, *Bull. Amer. Meteor. Soc.*, 66, 437-440, 1985

736   Heymsfield, A.J., L.M. Miloshevich, Homogeneous ice nucleation and

737 supercooled liquid water in orographic wave clouds, *J. Atmos. Sci.*, 50, 2335–2353, 1993

738   Heymsfield, A.J., P.R.Field, M.Bailey, D.Rogers, J.Stith, C.Twohy, Z.Wang, and

739   S. Haimov, Ice in Clouds Experiment—Layer Clouds. Part I: Ice Growth Rates Derived

740   from Lenticular Wave Cloud Penetrations. *J. Atmos. Sci.*, 68, 2628–2654, 2011

741   Khain, A.P., M. Ovtchinnikov, M. Pinsky, A. Pokrovsky and H. Krugliak, Notes

742   on the state-of-the-art numerical modeling of cloud microphysics. *Atmos. Res.*, 55,159–

743   224, 2000

744   Korolev, A.V. and G.A.Isaac, Shattering during sampling by OAPs and HVPS.

745   Part I: Snow particles, *J. Atmos. Oceanic Tech.*, 22, 528-542, 2005

746   Korolev, A.V., E. F. Emery, J. W. Strapp, S. G. Cober, and G. A. Isaac,

747   Quantification of the effects of shattering on airborne ice particle measurements, *J.*

748   *Atmos. Oceanic Technol.*, 30, 2527–2553, 2013

749   Lawson, R.P., and W.A. Cooper, Performance of some airborne thermometers in

750   clouds, *J. Atmos. Oceanic Tech.*, 7, 480-494, 1990

751   Meyers, M.P., P.J. DeMott, and W.R. Cotton, New primary ice-nucleation

752   parameterizations in an explicit cloud model, *J. Appl. Meteor.*, 31, 708–721, 1992

753   Muhlbauer, A. and U.Lohmann, Sensitivity studies of aerosol–cloud interactions

754   in mixed-phase orographic precipitation, *J. Atmos. Sci.*, 66, 9, 2009

755   Murray, B.J., D. O'Sullivan, J.D.Atkinson and M.E. Webb, Ice nucleation by

756   particles immersed in supercooled cloud droplets, *Chem. Soc. Rev.*, 41, 6519-6554, 2012

757   Niemand, M., O. Möhler, B. Vogel, H. Vogel, C. Hoose, P. Connolly, H. Klein, H.

758   Bingemer, P. DeMott, J. Skrotzki and and T.Leisner, A particle-surface-area-based

759   parameterization of immersion freezing on desert dust particles, *J. Atmos. Sci.*, *69*, 3077–

760   3092, 2012

761   Parish, T.R., and D.Leon, Measurement of Cloud Perturbation Pressures Using an

762   Instrumented Aircraft, *J. Atmos. Oceanic Technol.*, 30, 215–229, 2013

763   Pokharel, B., G. Vali, Evaluation of collocated measurements of radar reflectivity

764   and particle sizes in ice clouds, *J. Appl. Meteorol.*, 50, 2104-2119, 2011

765   Pratt, K.A., P.J.DeMott, J.R.French, Z.Wang, D.L.Westphal, A.J.Heymsfield,

766   C.H.Twohy, A.J.Prenni, and K.A.Prather, In situ detection of biological particles in cloud

767   ice-crystals, *Nat. Geosci.*, 2, 398-401, 2009

768   Rodi A.R. and P.A.Spyers-Duran, Analysis of time response of airborne

769   temperature sensors, *J. Appl. Meteorol.*, 11, 554-556, 1972

770   Rogers, R.R. and M.K. Yau, *A Short Course in Cloud Physics*, 3rd ed. Permagon

771   Press, 304 pp., 1989

772   Rogers, D.C., P.J.DeMott, S.M.Kreidenweis and Y.L.Chen, A continuous-flow

773   diffusion chamber for airborne measurements of ice nuclei, *J. Atmos. Oceanic Technol.*,

774   18, 725-741, 2001

775   Richardson, M.S., P.J. DeMott, S.M. Kreidenweis, D.J. Cziczo, E.J. Dunlea, J.L.

776   Jimenez, D.S. Thomson, L.L. Ashbaugh, R.D. Borys, D.L. Westphal, G.S. Casuccio and

777   T.L. Lersch, Measurements of heterogeneous ice nuclei in the western united states in

778   springtime and their relation to aerosol characteristics, *J. Geophys. Res.*, 112, D02209,

779   2007

780   Snider, J.R., and M.D. Petters , Optical particle counter measurement of marine

781   aerosol hygroscopic growth, *Atmos. Chem. Phys.*, 8, 1949-1962, 2008

782   Snider, J.R., D. Leon and Z. Wang, Southeast pacific stratocumulus cloud droplet

783   concentrations. Part I – Modeled, retrieved, and directly-observed values, submitted to

784   the *J. Atmos. Sci.*, 2014

785   Strapp, J.W., W.R. Leaitch and P.S.K. Liu, Hydrated and dried aerosol-size-

786   distribution measurements from the particle measuring systems FSSP-300 probe and the

787   deiced PCASP-100x Probe, *J. Atmos. Oceanic Tech.*, 9, 548-555, 1992

788   Strapp, J.W., F.Albers, A.Reuter, A.V.Korolev, U.Maixner, E.Rashke and

789   Z.Vukovic, Laboratory measurements of the response of a PMS OAP-2DC, *J. Atmos.*

790   *Oceanic Tech.*, 18, 1150-1170, 2001

791   Wang, Z. and K. Sassen, Cloud type and macrophysical property retrieval using

792   multiple remote sensors, *J. Appl. Meteor.*, 40, 1665–1682, 2001

793   Wang, Z., P. Wechsler, W. Kuestner, J. French, A. Rodi, B. Glover, M. Burkhart

794   and D. Lukens, Wyoming Cloud Lidar: instrument description and applications, *Opt.*

795   *Express*, 17(16), 13576-13587, 2009

796   Wang, Z., J. French, G. Vali, P. Wechsler, S. Haimov, A. Rodi, M. Deng, D. Leon,

797   J. Snider, L. Peng, Single aircraft integration of remote sensing and in situ sampling for

798   the study of cloud microphysics and dynamics, *Bull. Am. Meteorol. Soc.*, 93, 653-668,

799   2012

800   Westbrook, C.D. and A.J. Illingworth, The formation of ice in a long-lived

801   supercooled layer cloud, *Quart. J. Roy. Meteor. Soc.*, 139, 2209-2221, 2013

802   Wright, T. P., M.D.Petters, J.D.Hader, T.Morton and A.L.Holder, Minimal

803   cooling rate dependence of ice nuclei activity in the immersion mode, *J. Geophys. Res.*

804   *Atmos.*, 118, 10,535–10,543, doi:10.1002/jgrd.50810, 2013

805   Vali, G. and E.J. Stansbury, Time-dependent characteristics of the heterogeneous

806   nucleation of ice, *Can. J. Phys.*, 44, 477-502, 1966

807   Vali, G., M.K.Politovich and D.G.Baumgardner, Conduct of cloud spectra

808   measurements, Report AFGL-TR-81-0122, Air Force Geoph. Lab., Available from Nat'l.

809   Techn. Inf. Serv., Order No. AD-A102944/6, 1981

810   Vali, G. and Snider, J. R., Time-dependent freezing rate parcel model, Atmos.

811   Chem. Phys. Discuss., 14, 29305-29329, doi:10.5194/acpd-14-29305-2014, 2014

812   Vali, G., Nucleation terminology, *Bull. Am. Meteorol. Soc.*, 66, 1426-1427, 1985

813   Vali, G., Interpretation of freezing nucleation experiments: Singular and

814   stochastic; sites and surfaces, *Atmos. Chem. Phys. Discuss.*, 14, 1711-1760, 2014

815   Young, H.D., *Statistical Treatment of Experimental Data*, McGraw-Hill Book

816   Company, pp. 107, 1962